The signature of geomagnetic field external drivers in Swarm data

D. Saturnino[1,2], M. A. Pais[2,3], J. Domingos[2,3]

[1]Laboratoire de Planétologie et Géodynamique, UMR-6112, CNRS, Université de Nantes, Université d'Angers, France
[2]Univ. Coimbra, CITEUC, Geophysical and Astronomical Observatory, Coimbra, Portugal
[3]Univ. Coimbra, Department of Physics, Coimbra, Portugal

Key Points:

- Dense grid of external field series computed at Virtual Observatories from Swarm data, with 30-days time resolution
- PCA tools recover a dominant zonal dipolar mode with sub-annual variability strongly correlated with geomagnetic activity indices
- A less well-resolved mode shows a nearly equatorial wavenumber-4 structure that peaks at the equinoxes

Corresponding author: Diana Saturnino, diana.saturnino@univ-nantes.fr

Abstract

The separation of contributions from different sources in the magnetic field signal measured at satellite altitude is an open challenge. An approach to this problem, using Principal Component Analysis, is here applied to geomagnetic external field series at Virtual Observatories (VO). These series are computed from an enlarged dataset of Swarm data covering all local times and all geomagnetic activity levels between January 2014 and December 2019. For each 30-days time window, the Equivalent Source Dipole technique is used to reduce all measurements inside a cylinder to one single 'observation' at its axis and 500 km altitude. Our results reveal a first principal mode with dipolar geometry and time variation following very closely the RC-index of geomagnetic activity. They display a resolved second principal mode with annual periodicity and of approximately zonal quadrupolar radial pattern, reminiscent of results in a previous study using VO series from a filtered satellite dataset and with lower time resolution. We resort to the recent comprehensive model CM6 to identify a possible source for this second mode. We propose that the dipolar mode is the expression of the magnetospheric ring current dynamics, at 30-day time resolution, and the quadrupolar mode is the expression of the annual asymmetry between local summer and winter Sq current vortices. Two fainter modes could be related to the equinoctial amplification of Sq vortices and the ionospheric dynamo modulation by nonmigrating tides. We show that a more uniform local time sampling could contribute to better resolve ionospheric structures.

1 Introduction

Time variations observed from a satellite are due both to local variations with time and to spatial variations along the satellite trajectory. This is quite different from on-Earth observatories, whose series describe local time variations. In search for series obtained from satellite data that could be more easily compared with magnetic observatory series, and treated using the same kind of mathematical tools, Mandea and Olsen (2006) developed the idea of Virtual Observatories (VO). Each VO measurement averages satellite data inside a certain volume, typically a cylinder, and during a specific time window, typically one (Mandea & Olsen, 2006; Beggan et al., 2009; Hammer et al., 2021) or four (Shore, 2013; Hammer et al., 2021) months duration.

A local Cartesian cubic potential description has been initially used by Mandea and Olsen (2006) to compute the field value at each target VO position, a method that has been followed by several other authors (Beggan et al., 2009; Shore, 2013; Barrois et al., 2018). This is also the approach followed in GVO (Geomagnetic Virtual Observatories) products of ESA Swarm DISC international consortium (Hammer et al., 2021). Using this method, Hammer et al. (2021) recently computed GVO series of monthly values with no data selection, at 490 km altitude. Saturnino et al. (2018) showed that it is possible to use the Equivalent Source Dipole (ESD) potential description (e.g. Mayhew, 1979; Langlais et al., 2004), to locally reduce all satellite measurements within each cylinder and a certain time interval, to a constant altitude and a mean epoch. Starting from the magnetic anomaly created by a single magnetic dipole and using the superposition principle, a distribution of dipoles inside the Earth is sought that can explain a smooth field inside each cylinder, locally derived from a Laplacian potential.

Most previous studies that used satellite data to build VO series implemented a strict selection whereby only quiet, local night-time measurements were kept in the analysis (Mandea & Olsen, 2006; Barrois et al., 2018; Domingos et al., 2019; Hammer et al., 2021). This was intended to capture short time variations of the internal signal. Such selection is accomplished by using threshold values for proxies of geomagnetic activity as indices Kp, Dst or, more recently, the RC index (Olsen et al., 2014). Beggan et al. (2009) showed how, by relaxing selection constraints, external signals come to influence SV models and inverted core flows. This discussion was resumed by Shore (2013), who

suggested to remove models' estimations of magnetospheric and ionospheric contributions from Swarm data, as a means to isolate the internal field in VO series. (Domingos et al., 2019) showed that, even after subtracting the magnetospheric contribution from CHAOS-6 (Finlay et al., 2016) and the ionospheric contribution from CM4 (Sabaka et al., 2004), an external imprint of quasi-annual periodicity still remained.

At satellite altitude the main sources of external fields are the magnetospheric currents flowing above the spacecraft, ionospheric currents flowing below and field-aligned currents connecting the two regions. The magnetospheric currents of importance are the ring current, the partial ring current and the magneto-tail current (Lühr et al., 2017). At low and mid latitudes, the ionospheric currents are mostly present in the dayside hemisphere due to the E-dynamo, and are responsible for the well-known daily variation commonly referred to as solar quiet (Sq) variation. Besides, there is a strong azimuthal current in the dayside known as the equatorial electrojet (EEJ). In the F-region, large winds exist also, that have a dominant effect at night when the E-region conductivity is low. Finally, there are interhemispheric field-aligned currents connecting the Sq vortices in the two hemispheres (Yamazaki & Maute, 2017; Park et al., 2020). E and F-region dynamos are known to be coupled to lower atmosphere tides, so that certain space-time features related to the neutral atmosphere behaviour can be seen in the ionospheric external field (Oberheide & Forbes, 2008; Lühr et al., 2008; Pedatella et al., 2011; Chulliat et al., 2016).

An accurate representation of external fields' spatial and temporal variation is crucial in field modelling source separation. However, most available geomagnetic field models are computed using rigid data selection criteria and their validity is limited to low activity periods. As a result, external fields may be underestimated (Lühr & Zhou, 2020). A non-parametric method as PCA may be used as an exploration method, to help to identify components that are present in the data although absent or under-represented in the models.

Domingos et al. (2019) worked on a set of VO series built from Swarm data by Hammer (2018). Applying Principal Component Analysis (PCA), the total signal was decomposed into decorrelated modes. Among these, the separation was made between modes from internal and external sources. The best resolved external mode showed annual time oscillation and zonal quadrupolar geometry in the radial component chart, which was not given a physical explanation. No mainly dipolar mode with a timescale variation possibly related with external sources was retrieved in their analysis. PCA and similar methods have been previously employed to separate variability modes in the external geomagnetic field or external equivalent currents (e.g. Yamazaki et al., 2009; Shore et al., 2016).

In this study, using a dense and uniform distribution of VOs computed from Swarm satellite data ('Data for VO series'), we look for a better definition of the main PCA external modes ('Method'). As in Saturnino et al. (2018), VO series are computed using all available satellite measurements obtained inside each elemental volume during a given time period, with no attempt to remove the external field contribution. Both the geographic and centered-dipole frames are tested, in search for the reference frame where resolution of external modes is the best ('Results'). The spatial and temporal functions of each external mode are compared against models and proxies for external signals ('Characterization of main external modes at satellite altitude'). In the end, we provide a physical interpretation for the two main, external resolved modes ('Discussion'). We also discuss a third and fourth modes, possibly related to the semi-annual oscillation of solar quiet current vortices and the ionospheric dynamo modulation by nonmigrating tides.

2 Satellite orbit periodicities

An overview of periodicities that are present in the sampling by satellites along their orbit, and that may affect VO series is given below. ESA's Swarm mission, launched on 22 November 2013, consists of a constellation of three identical satellites in nearly polar orbits at different altitudes (Friis-Christensen et al., 2006). By April 2014, two of them (A and C, inclination i=87.3°) were flying at about h=460 km altitude, with 1.4° separation in longitude at the equator, and the third satellite (B, i=87.7°) was flying about 50 km higher. The average orbital period of these satellites is $\sim$ 95 min, leading to 15 crossings of the equator by the ascending node, each 24 hours. As a result of precession of satellite orbit planes around the Earth rotation axis, and the rotation of the Earth around the Sun, the Local Time of Ascending Node (LTAN) of each satellite is continuously drifting. The drift period of the satellite, T_S, is computed from other orbit parameters as altitude h above Earth's surface, and inclination i of the orbit plane, through

$$T_S = \frac{365.25}{10.11 \left(\frac{R_E}{R_E + h} \right)^{7/2} \cos i + 1} \quad , \tag{1}$$

where R_E is the Earth's radius (e.g. Capderou, 2005). It takes a period of $\sim$ 9 months for the LTAN of Swarm satellites to complete a full 24h (retrograde) cycle (Montenbruck & Rodríguez, 2020; Chulliat et al., 2016). This is shown in Figure 1, where the more slowly drift in the orbit plane of the B satellite relative to the other two is also perceived (9.2 months against 8.8 months, in the beginning of the mission). For all locations, two local time (LT) bands with 12 hour separation are monitored by the satellites, each day. The LT bandwidth covered at each day/night hemispheres at each passage changes with time, due to different LTAN drift velocities for A+C and B satellites (see Figure 1). The B satellite, which at the beginning of Swarm mission covers the same LT as the other two satellites leading to more localised LT coverage (until about the middle of 2015), gradually separates from A+C and moves closer to an orthogonal configuration. During about two years from the beginning of 2017 to the end of 2018, a full coverage is reached. Then, the B satellite LT band moves closer to A+C, again, and the whole cycle repeats. Comparing LT coverage at the end of 2019 and middle of 2016 (note the symmetry), it is expected that it will take more 2.5 years, approximately, to close the cycle and attain the same configuration as by January 2014. This means an amplitude modulating periodicity of about 8.5 years. The $\sim$ 9 months periodicity for the LTAN drift is larger than the time to cover all the 24 local times, since during each satellite orbit the Local Time of Descending Node (LTDN) is LTAN+12. For this reason, the fundamental periodicity related with LT day/night coverage is $\sim$ 4.5 months (Bezděk et al., 2017). As the external geomagnetic activity depends on LT, the oscillation between dominantly day and night LTs introduces this periodicity in the observed magnetic field, as a sampling effect (e.g. Beggan et al., 2009; Shore, 2013). This will be further discussed in 'Results' and 'Discussion'.

3 Data for VO series

The raw data used in this study consists of 1-s measurements of the geomagnetic field geocentric components (X, Y, Z) from ESA's Swarm Level L1b data product, baseline version 0505 (0506 for some data files). Data from all three Swarm satellites (A, B and C) were considered, for the period between January 2014 and December 2019. Data were screened for quality flags defined in the Level 1b Product Definition Document (Toffner-Clausen & Nielsen, 2018). Only measurements identified as being in nominal mode were kept. Note that Swarm C data after 5th November 2014 was used, i.e. when the ASM scalar field instrument stopped working, as the C satellite vector data can be corrected using Swarm A ASM data. No data selection based on the geomagnetic activity was applied to the dataset.

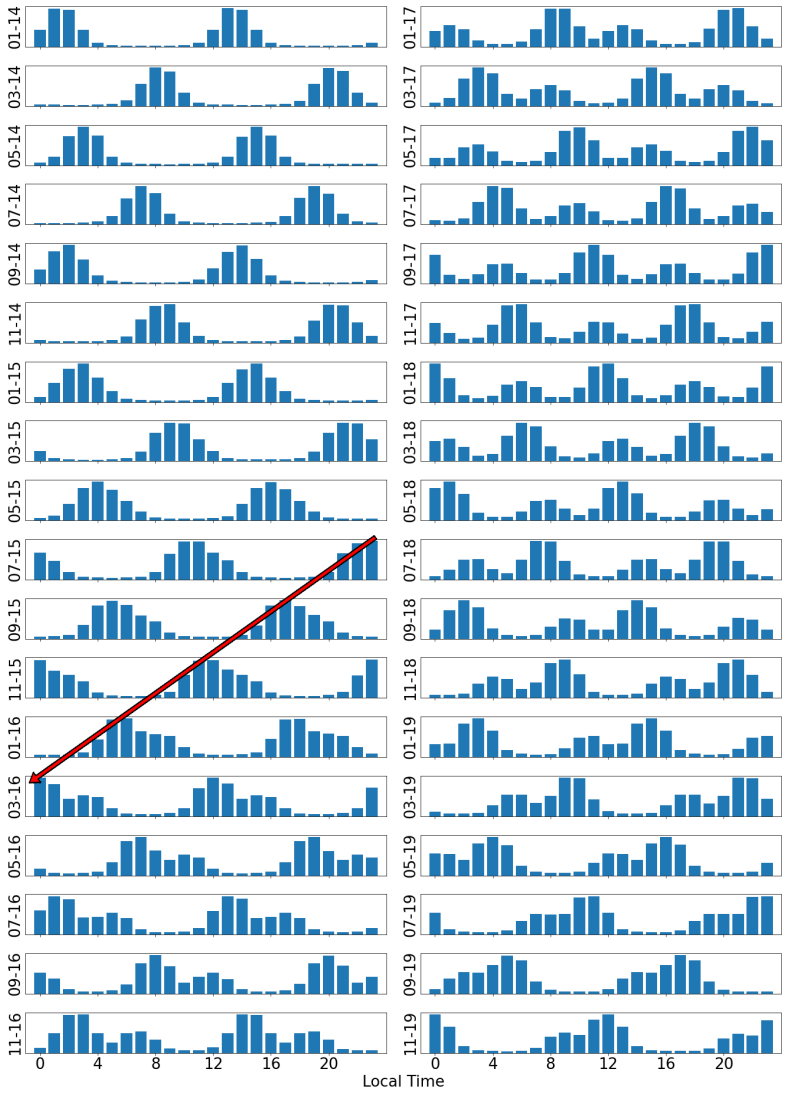

Figure 1. Local time drift of Swarm satellites A+B+C. Variation in time of local time distribution of the whole set of satellite measurements used in the calculation of VO series, during the 2014 to 2019 time period (only 1 out of 2 epochs is plotted, with 1 epoch corresponding to a 30-day period). Straight red line shows the retrograde drift of a certain group of sampled LT values.

4 Method

This section describes the approach to derive the VO time series and analyse them, and an overview is presented in Figure 2. As is shown there, a similar procedure is applied in two distinct reference frames, the geocentric (GEO) or ECEF (Earth-centered Earth-fixed) and the centered-dipole (CD) frames, consisting in the following steps: i) preparing the satellite data, by grouping them into spatial and temporal bins; ii) applying ESD inversion to compute VO series in a mesh; iii) subtracting a main field (MF) model from VO series of the total field; iv) applying PCA to the remaining series. For proper definition of the reference frames in use, see Laundal and Richmond (2017). We

may expect that distinct external sources show higher symmetry in different reference frames, so this rotation may help to separate external modes.

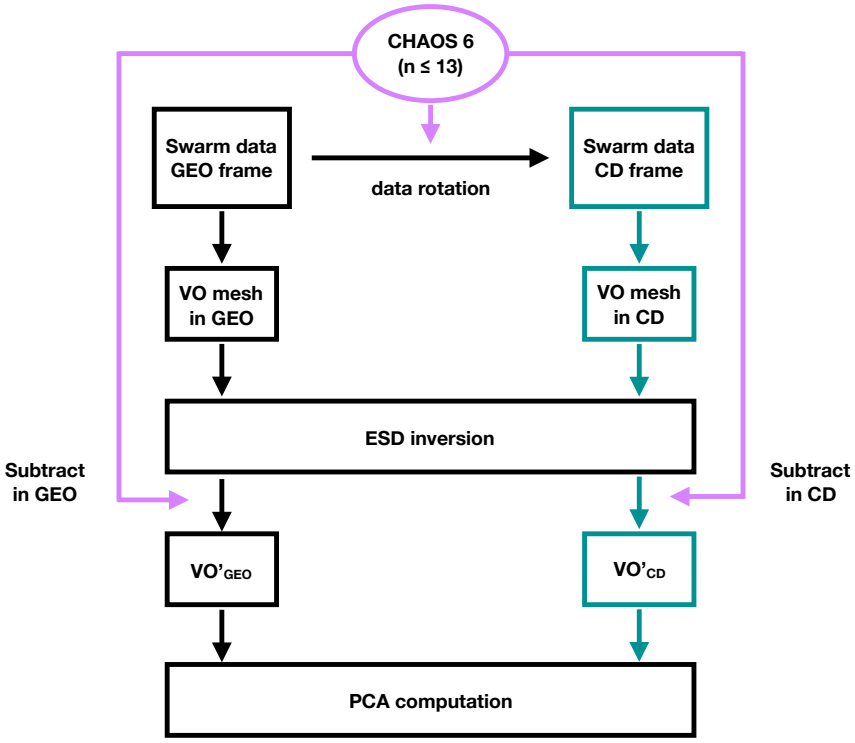

Figure 2. Overview of the approach followed in this study.

4.1 VO-ESD inversion

The Equivalent Source Dipole (ESD) technique is based on the expression of the magnetic field potential V at point P with spherical coordinates (r, θ, ϕ), due to a magnetic point dipole of moment $\mathbf{M}$ at a point with coordinates (r_d, θ_d, ϕ_d). Point P is outside the region where dipoles are distributed. Then

$$V = -\frac{\mu_0}{4\pi}\mathbf{M} \cdot \nabla \left(\frac{1}{l}\right) \quad , \tag{2}$$

where l is the distance between the dipole and point P, and the magnetic field is obtained from $\mathbf{B} = -\nabla V$. A distribution of several dipoles is required to fit the observed field $\mathbf{B}(P)$. A linear relation can be written between the measured components of the field and the vector moments of the dipoles which, once inverted for the equivalent dipole sources, can be used to find the field at any point inside the cylinder. No particular physical meaning is attributed to the number, location, orientation or magnitude of these dipoles. The approach was originally set up by Mayhew (1979) and the implementation in our study follows those by Purucker et al. (1996), Dyment and Arkani-Hamed, Langlais and Purucker (2007) and, more recently, Oliveira et al. (2015) for Mercury, using MESSENGER data, and Saturnino et al. (2018) for the Earth, using Swarm data. The ESD method was chosen to reduce an ensemble of magnetic measurements to a single point. This is a mathematical technique to fit a Laplacian potential to the data, in the same way as the Cartesian potential model in, e.g., Hammer et al. (2021). It has the relative advantage of being applied directly to total Swarm data values instead of residuals after removing a MF model, and of using the same coordinate reference frame for all cylinders

(spherical Earth-centered coordinates). The method has been previously tested and shown to be effective in Saturnino et al. (2018).

To obtain the VO field values using the ESD method (VO-ESD), a global mesh of VOs was constructed, following Saturnino et al. (2018) but for a sparser mesh (larger cylinders). Two different reference frames were considered (see Figure 2). In one case, the set of VO coordinates was fixed in time relative to the GEO frame. In the other, the whole satellite dataset were rotated to the CD frame, a different rotation for each 30-day period (an epoch) and using the CHAOS-6 model to compute the rotation angles (θ_0, ϕ_0) where $\theta_0 = \arccos(-g_1^0/m)$, $\phi_0 = \arctan 2(-h_1^1, -g_1^1)$ and $m = \sqrt{(g_1^0)^2 + (g_1^1)^2 + (h_1^1)^2}$. The rotation was made prior to the choice of the VOs grid, so that this second grid is fixed relative to the changing CD frame, although its nodes are never exactly at the same geographic locations from one epoch to the other.

In each reference frame, the Swarm data (after quality screening) was grouped into cylinders and, within each cylinder, into M=72 different epochs of 30 days each, in the period from January 2014 to December 2019. For each epoch, an approximately equal area mesh was obtained with the VO locations at 500 km altitude and separated in latitude by 3.5°. The central-most band is located at latitude $\Theta_{VO} = -0.75°$, with the other bands in the Southern Hemisphere (SH) lying at $\Theta_{VO} = -4.25°, -7.75°, ..., -88.25°$. In the Northern Hemisphere (NH), VOs are placed at $\Theta_{VO} = 2.75°, 6.25°, ..., 86.75°$. In each band, the number of longitudinal divisions $N_{\Theta_{VO}}$ (rounded up to the nearest integer) is chosen so that:

$$N_{\Theta_{VO}} = \frac{360}{3.5} \cos \Theta_{VO}. \tag{3}$$

Hence, immediately north and south of the equator (geographic or geomagnetic) there are 103 virtual observatories, around 45° latitude there are 74 and, closest to the poles, only 3 (SH) or 6 (NH). The resulting mesh contains $N_P = 3394$ VOs. The data for each VO consists of all data acquired inside a cylinder of 2.0° (i.e., about 240 km) radius centered at each VO and during a 30-day period. Depending on the epoch, satellite data within each cylinder lie between 450 and 530 km altitude (Swarm satellite's altitude range). 500 km was chosen as the common altitude for all VOs, as it is a round number close to the mean altitude of all Swarm data.

The VO-ESD inversion was applied following closely Saturnino et al. (2018), both in the GEO and CD reference frames. In order to gather a minimum number of satellite data values inside each cylinder, needed to correctly estimate the parameters in the inversion, a period of 30 days was used. For each epoch and each cylinder vector dataset, the equivalent magnetisation of dipoles placed at 2900 km in the Earth's interior was sought by a least-squares fit in an iterative, conjugate gradient, inversion scheme (Purucker et al., 1996). Then, the forward calculation was used to estimate a magnetic field value at the cylinder axis and 500 km altitude.

Although the VO-ESD inversion makes no parametrization of external contributions, they are expectedly present in VO series (e.g. Oliveira et al., 2015; Saturnino et al., 2018). The magnetic field of internal origin ($n \leq 13$) as given by the CHAOS-6 model (Finlay et al., 2016, version CHAOS-6-x9) was subtracted from the VO time series, in order to isolate the external contribution. For the CD frame, the CHAOS-6 coefficients were also rotated before the MF contribution was removed. The lithospheric field was not subtracted, since it has no contribution for the time variability of the field during the (short) time interval 2014–2019. The two sets of VO time series residuals, after subtracting a MF model, are called VO'$_{GEO}$ and VO'$_{CD}$.

4.2 PCA decomposition

The set of VO' series was stored into a matrix $\mathbf{X}$, each row with data from a given epoch, with $M = 72$ distinct epochs. Three sets of $N_P = 3394$ columns were concate-

nated, each set containing a given component of the field at all VOs. The PCA analysis decomposes the data matrix $\mathbf{X}$ into a sum of principal components (or modes) j, with spatial patterns $\mathbf{p}^j$ (the Empirical Orthogonal Functions, EOFs) multiplied by time series $\mathbf{y}^j$ (the Principal Components, PCs), according to:

$$\mathbf{X} = \sum_{j=1}^{k} \mathbf{y}^j \otimes \mathbf{p}^{j\,T} = \sum_{j=1}^{k} \alpha^j \mathbf{y'}^j \otimes \mathbf{p}^{j\,T}, \tag{4}$$

where $\mathbf{y'}^j$ and $\mathbf{p}^j$ are orthonormal in the sense that $\mathbf{y'}^{j\,T}\mathbf{y'}^i = \delta_{i,j}$ and $\mathbf{p}^{j\,T}\mathbf{p}^i = \delta_{i,j}$. α^j are non-negative scalars, the singular values of data matrix $\mathbf{X}$, and $\otimes$ represents the dyadic product. A further parameter characterising the variance of each mode is $\lambda^j = (\alpha^j)^2/(M-1)$. λ^j values can be directly obtained as the eigenvalues of $\mathbf{X}^T\mathbf{X}/(M-1)$. k is the number of modes that explain most of the signal variance, the remaining modes being usually identified as noise. The notation in use is the same as in Domingos et al. (2019), where a more detailed description of the PCA method, as applied here, can be found.

The PCA decomposition was applied to the whole set of VO'$_{GEO}$ and VO'$_{CD}$ series. For each VO, the three series of magnetic field components (B_r, B_θ, B_ϕ) were used as additional parameters in the spatial dimension, assuming the same time variation associated to the three of them (Shore et al., 2016).

Rotating the whole dataset by a single set of (θ_0, ϕ_0) angles would not change the result in terms of PCA modes: the EOF spatial structures would be the same in the rotated frame as in the initial frame, only rotated; their time variation would be given by exactly the same time series (e.g. Jolliffe, 2002). However, as applied here, the rotation angle is changing with the MF, even if only slightly, and the modes are no longer exactly the same.

4.3 Geomagnetic activity proxies and model CM6

An explanation for the origin of the main PCA modes was sought using solar and geomagnetic activity proxies, as well as resorting to the recent comprehensive CM6 model (Sabaka et al., 2020).

Different series of parameters used as proxies of Sun-Earth interaction were compared with the PC time functions from our analysis. Daily averages were downloaded from OMNI database for i) the solar activity index F107 (the solar radio flux at 10.7 cm wavelength) and the sunspot number R; ii) the interplanetary magnetic field components in the GSM coordinate system, B_x, B_y and B_z; iii) the solar wind plasma velocity V_{sw} and iv) the geomagnetic activity indices Kp, ap, Dst. Minute values of Auroral Electrojet indices SML, SMU and SME (Gjerloev, 2012; Newell & Gjerloev, 2011) were downloaded from SuperMAG database. The RC index, which monitors the strength of the magnetospheric ring current, was downloaded from DTU webpage. Finally, the Newel coupling function (Newell et al., 2007) was computed from downloaded parameters. For each of these parameters, averages were computed over the same 30-day epochs considered in the VO-ESD inversion and then correlated with the main PCs.

The CM6 model was used to retrieve general spatial patterns for modes related with the ionospheric variability. To this end, 30-day resolution time series were produced at the VOs mesh positions, fixed in the GEO reference frame. These series were obtained as follows: 30-days mean values were computed from hourly values of the total ionospheric contribution (primary plus induced contributions) as given by CM6 model for the period January 2014 to December 2019, resulting in 72-points time series at each VO location. The PCA analysis was applied to the simulated dataset.

5 Results

5.1 VO series

The VO mesh and the distribution of satellite data among cylinders can be a source of spatial or temporal asymmetries. The presence of spatial patterns and time signals possibly related with such sampling asymmetries was checked, so that they could be later recognized in the computed PCA modes.

The high density of cylinders allows to have a very good spatial coverage. However, it implies that a subset of data inside each cylinder is used to constrain the ESD models in more than one cylinder simultaneously. In a first test (not shown), we computed the spatial distribution of this oversampling and found that about 20% of data inside each cylinder is being used to constrain the ESD models inside neighbouring cylinders. We could not identify any spatial pattern similar to the main EOFs of the PCA applied to VO geomagnetic series. Furthermore, the use of a subset of data values to constrain the ESD models in different (neighbouring) regions simultaneously is not seen as a drawback, as it is very homogeneously distributed and promotes the continuity in the field between those regions.

A second check test was done (also not shown), to assess the distribution of the asymmetry in local day/night duration (where 'day' and 'night' refer to time after and before sunrise), and consequent aliasing of external magnetic field activity as discussed by Beggan et al. (2009) and Shore (2013). For each cylinder and each epoch it was computed the difference in the number of Swarm data values lying in the lit and dark LT intervals, in an attempt to parametrize the local day/night asymmetry. Then, PCA was applied to the space-time distribution of those differences. This asymmetry changes over time, as expected due to the obliquity of the Earth but also to the drift of the three satellite orbital planes (see Figure 1). The 1-year and 4.5 months periodicities can be retrieved. Nonetheless, at a given epoch, we could not see spatial patterns in the day/night asymmetry, similar to the main EOFs retrieved in the PCA analysis of VO geomagnetic series (see section 6).

Although not dominant in the spatial structures of the computed PCA main modes, the day/night asymmetries due to the sampling along the satellite orbits are present in the VO-ESD inversion. Computed ESD estimations, inside each cylinder, explain the Swarm satellite data with a RMS misfit distribution shown in Table 1. This misfit is computed from comparison of estimated and observed total field values and using all Swarm data inside each cylinder. The spatial distribution of RMS misfit for the three components, shown in Figure 3 for epoch centered on 2018.8 in the GEO frame, shows sectorial banding, typically of order 15 and mainly in the meridional component. A similar result was also retrieved by Beggan et al. (2009), who noticed it was closely related to the presence of external contributions and would be much weaker when using filtering constraints on the selected data. Shore (2013) confirmed these findings, making it clear that it was due to aliasing of the external activity due to sampling along a drifting satellite orbit.

The plots of observed series at the ground level and VO-ESD series 500 km above can be seen in Figure 4 for the four observatories of COI (Coimbra, Portugal), CLF (Chambon-la-Forêt, France), HER (Hermanus, South Africa) and LRM (Learmonth, Australia). The MF contribution from CHAOS-6 model (up to spherical degree 13) has been subtracted from both on-ground observations and from the VO-ESD series. Note that the ESD inversion is applied to Swarm total field data, contrary to other studies where the inversion inside each cylinder is applied to deviations of Swarm data relative to a MF model (e.g. Hammer et al., 2021). So the retrieval of correlated oscillations at the ground level and at height is an indirect indication that the MF contribution is correctly computed using ESD (see also Saturnino et al., 2018). The signal represented by black and blue curves is expected to be due to i) the lithospheric field; ii) a MF contribution not accounted

GEO Frame			CD Frame		
Global ($\|\Theta_{VO}\| \leq 60°$)			Global ($\|\Theta_{VO}\| \leq 60°$)		
B_r/nT	B_θ/nT	B_ϕ/nT	B_r/nT	B_θ/nT	B_ϕ/nT
10 **(7)**	22 **(16)**	20 **(12)**	9 **(6)**	21 **(14)**	19 **(10)**

Table 1. RMS misfit between Swarm data and VO-ESD estimations inside each VO cylinder, taking into account all VOs or just VOs with latitudes between ± 60° (in bold).

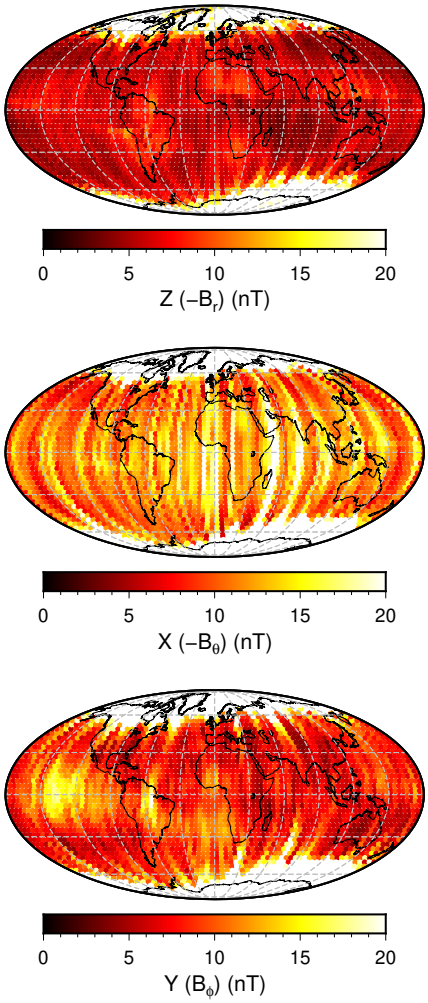

Figure 3. RMS misfit between Swarm data and VO-ESD estimations inside each VO cylinder, for the three components at epoch 2018.8, in the GEO frame.

for in CHAOS-6; iii) the external signal (both primary and secondary). There was no attempt to downward continue the VO series, as we don't know how the external field varies with altitude. The contribution from the lithospheric field is assumed constant during the 6 years time period, with a higher intensity on the ground (near the sources) than at 500 km altitude. This is in agreement with larger values for on-ground series in Figure 4. Results from the PCA analysis, discussed in section 6, do not support a relevant

MF contribution in series shown in Figure 4. Instead, the main four variability modes seem to be due to magnetospheric and ionospheric current sources. The VOs time series follow oscillations that are well correlated with series obtained on the ground, with higher correlations for X and Z than for Y components. Differences were expected, due to the fact that while the ionospheric contribution is seen from below at on-ground observatories, it is seen from above at VOs altitude. The highest values for the Pearson coefficient is 0.88 with a p-value less than 0.01, for component Z at CLF.

5.2 Principal modes

All 72 epochs were considered in the VO'$_{GEO}$ and VO'$_{CD}$ time series, when applying the PCA analysis. However, due to lower performance of the VO-ESD model at higher latitudes (see Table 1), only a subset of all VOs were used, namely those located at $|\Theta_{VO}| \leq 60°$, with Θ_{VO} defined in each reference frame, changing the VO number to $N_P = 2920$.

Figure 5 shows the singular spectrum, i.e. the variance of different modes as given by λ^j, in both reference frames. It also shows the standard error bars associated with each eigenvalue as given by North's rule of thumb (North et al., 1982). Mode 1 is responsible for around 30% of the data variability. Globally, the modes' variability is lower for VO'$_{CD}$ than for VO'$_{GEO}$. Modes 3 and 4, while degenerate in VO'$_{GEO}$, can be better resolved in the rotated CD frame. As an estimate for the noise level intensity above which PCA modes can be resolved, the PCA was applied to $M \times (3N_P)$ Gaussian random matrices of zero average elements and uniform standard deviation σ. The σ value was adjusted so that the first four eigenvalues computed from VO series rise above the Gaussian noise 'plateaux', for GEO and CD frames. These 'plateaux' are represented by the two straight lines shown in Figure 5 which connect eigenvalues for Gaussian random processes with $\sigma_{GEO} = 7.8$ nT and $\sigma_{CD} = 6.8$ nT. Interestingly, the difference of 1 nT between them is quite close (or even the same, for B_r) to corresponding differences in Table 1.

The PC time series are shown in Figure 6 for modes 1 to 4. The first mode has a sub-annual variability and a decreasing trend from 2015 onward. The second mode has a quasi-annual variability. Modes 3 and 4, both show clearly an oscillation of ~ 4.5 months, and an amplitude modulated by a period larger than 6 years (see Figure 1), possibly about 8.5 years (see section 2). The power spectra in Figure 6 help to better characterize the time variation of each mode. Periods of 4.5 and 9 months represent the time it takes for each satellite individually, as well as the A+C cluster, to recover the same sampling conditions regarding local times. The two different values account for the difference in sampling conditions depending if all local times are covered by either LTAN or LTDN, or by LTAN in particular. These two periods are clearly present in modes 2, 3 and 4. Also seen for these three modes, the spectral broadening between about 4 and 5 months, that can be explained due to the amplitude modulation of the 'carrier' period of ~ 4.5 months. Neither one of the periodicities related with uneven sampling of different local times is present in the main principal mode. This is indicative that mode 1 spreads over all local times i.e., is observed both during day and night LTs. Much on the contrary, modes 2, 3 and 4 reflect the dynamics of features bounded in a certain LT region. Those features are more clearly retrieved during epochs when the A+C sampling LT band (from the LTAN or the LTDN sides) is centered with them, and become more and more faint as the sampling LT band approaches an orthogonal configuration, where these modes reach minimum values. A semiannual period is dominant in mode 1 and relatively important in mode 3. It is also recovered in mode 4, if the PCA is applied in the CD reference frame. Finally, the annual oscillation is the period with the highest energy in mode 2, and is also present in modes 3 and 4.

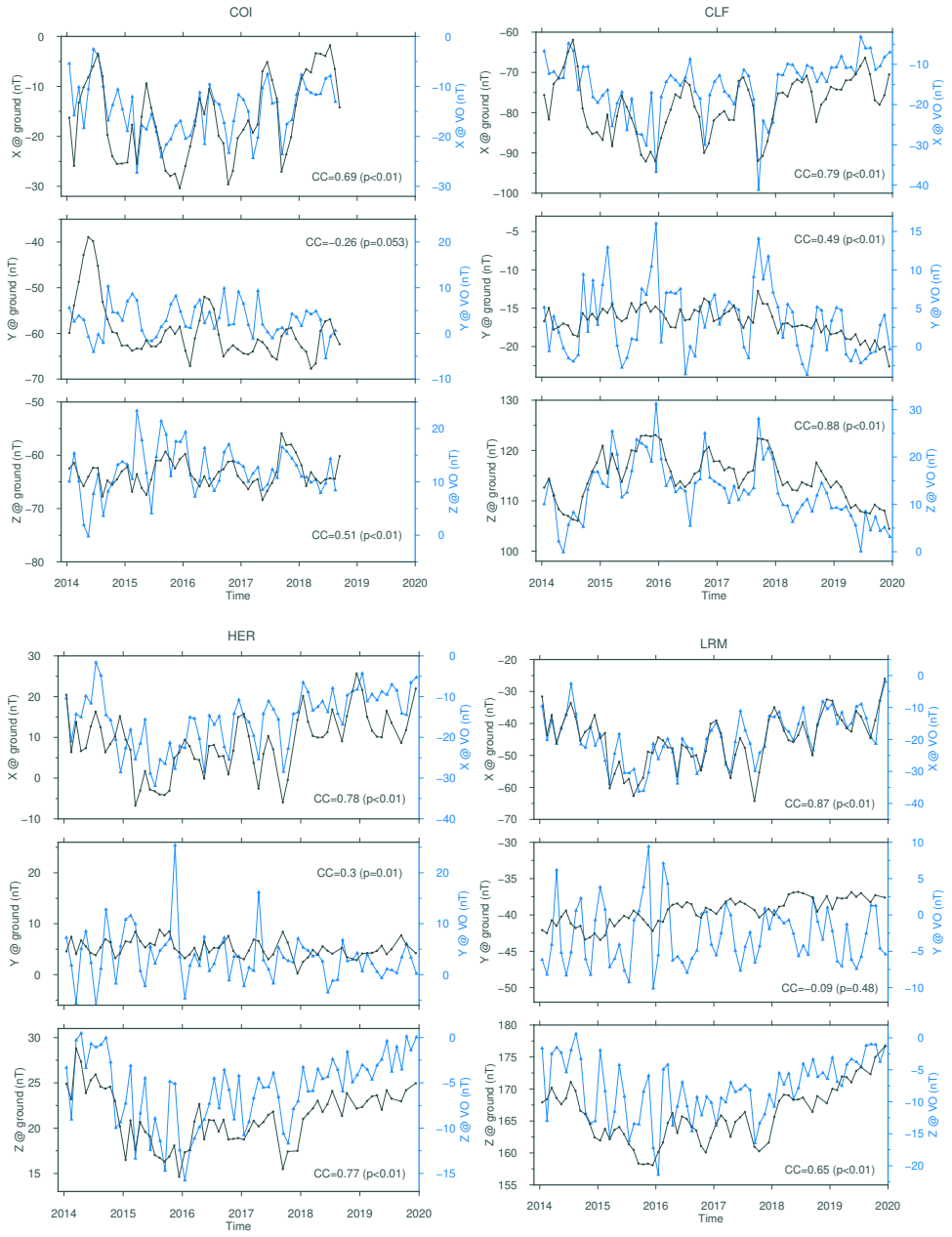

Figure 4. 30-day resolution time series for geomagnetic field components (X, Y, Z) at COI (40.03°N, 8.43°W), CLF (47.83°N, 2.26°E), HER (34.24°S, 19.23°E) and LRM (22.08°S, 114.10°E) observatories (grey) and at corresponding VOs at 500 km altitude (blue). For COI observatory, the series was interrupted at 2018.7, due to damages caused by hurricane Leslie at the variometers' house. Also shown inside each frame, the correlation coefficient (CC) between curves, and the corresponding p-value.

Figure 7 shows the spatial patterns (or EOFs) for each of the four modes and for the radial component, since this component is the best explained by the VO-ESD model (Table 1). The EOFs for VO'$_{CD}$ are approximately a rotated version of corresponding EOFs for VO'$_{GEO}$, as expected. While radial geomagnetic field charts of modes 1 and 3 have a dominantly dipolar symmetry, charts of modes 2 and 4 are mainly quadrupo-

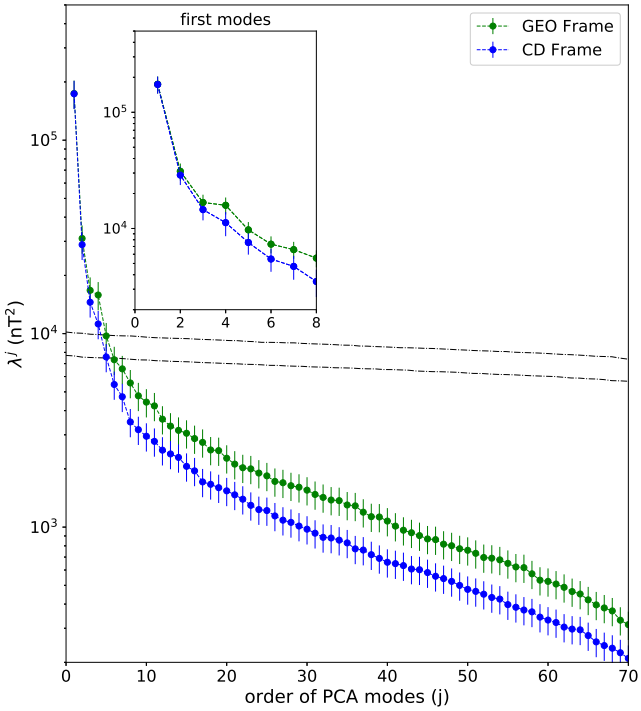

Figure 5. Singular spectra for VO'$_{GEO}$ and VO'$_{CD}$ datasets, in logarithmic scale. Error bars represent the standard error given by North's rule of thumb. The two straight lines are fitted to white Gaussian "noise" eigenvalues corresponding to $\sigma_{GEO} = 7.8$ nT and $\sigma_{CD} = 6.8$ nT.

lar. In particular for mode 1, the computation in the CD reference frame gives a more simple geometry. The equatorial oscillation over central America is smoothed out, which is exactly what is expected for a spatial pattern that is constrained by the tilted geomagnetic dipole, with inclination given by the MF degree-1 SH coefficients. The zonal symmetry further points toward a planetary and circular current system, which is also in agreement with the LT-invariance discussed previously. All together, our results align with the hypothesis that the magnetospheric ring current dynamics is present in mode 1. As for mode 2, it is not as clear wether the nearly equatorial spatial structures are more aligned with the GEO or with the CD equators. This may be an interesting result by itself, as it is known that low-latitude ionospheric current systems are constrained by both atmospheric tidal winds that are symmetric relative to the GEO equator and the ionospheric conductivity, symmetric relative to the CD equator (e.g. Pedatella et al., 2011). Finally, modes 3 and 4 also seem to include both symmetries, their source currents being probably more close to mode 2 than to mode 1.

Table 2 shows RMS values of the radial component for the first modes at peak epochs (different for each mode). Values are always smaller for the CD than the GEO reference frames, especially for mode 1 which seems to be due to a source current aligned with CD equatorial plane.

6 Characterization of main external modes at satellite altitude

The first 4 modes are now considered in detail, trying to identify possible mechanisms that could explain them. For modes 1 and 2, their power spectra and spatial patterns suggest that they display the dynamics of magnetospheric and ionospheric exter-

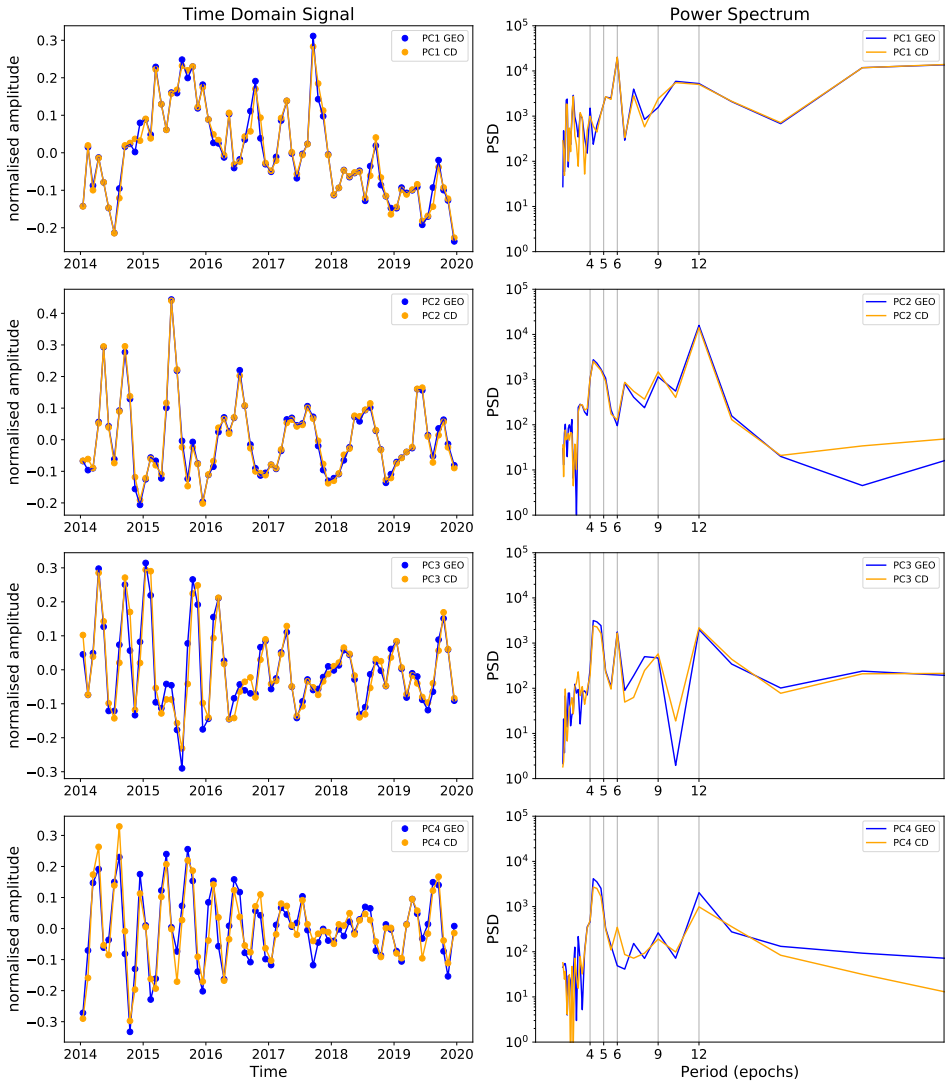

Figure 6. (Left) Normalized PC time series ($\mathbf{y}'^{j}$) for the first 4 modes, when applying PCA to V'$_{GEO}$ (blue) and V'$_{CD}$ (orange). j increases from top to bottom. (Right) Power spectra of each series.

nal sources, respectively, which we will now attempt to better characterize. As for modes 3 and 4, they exhibit as the main periodicity the 4.5 months it takes for Swarm constellation to cover all local times, especially during about the first two years of the satellite mission (see Figure 6). Also, as an amplitude modulator, a period larger than 6 years is present, possibly about 8.5 years, corresponding to the time it takes for the 3-satellite configuration to repeat again (see Figure 1).

6.1 Correlation with proxies of solar and geomagnetic activity

In a prospective search for the most direct sources of modes j =1, 2, 3 and 4, Figure 8 shows the Pearson correlation coefficient between time series $\mathbf{y}^j$ and different proxies of solar and geomagnetic activity. $\mathbf{y}^1$ time series shows the highest correlation (or anticorrelation) with RC, closely followed by the Kp/ap and SML/SME indices; neither

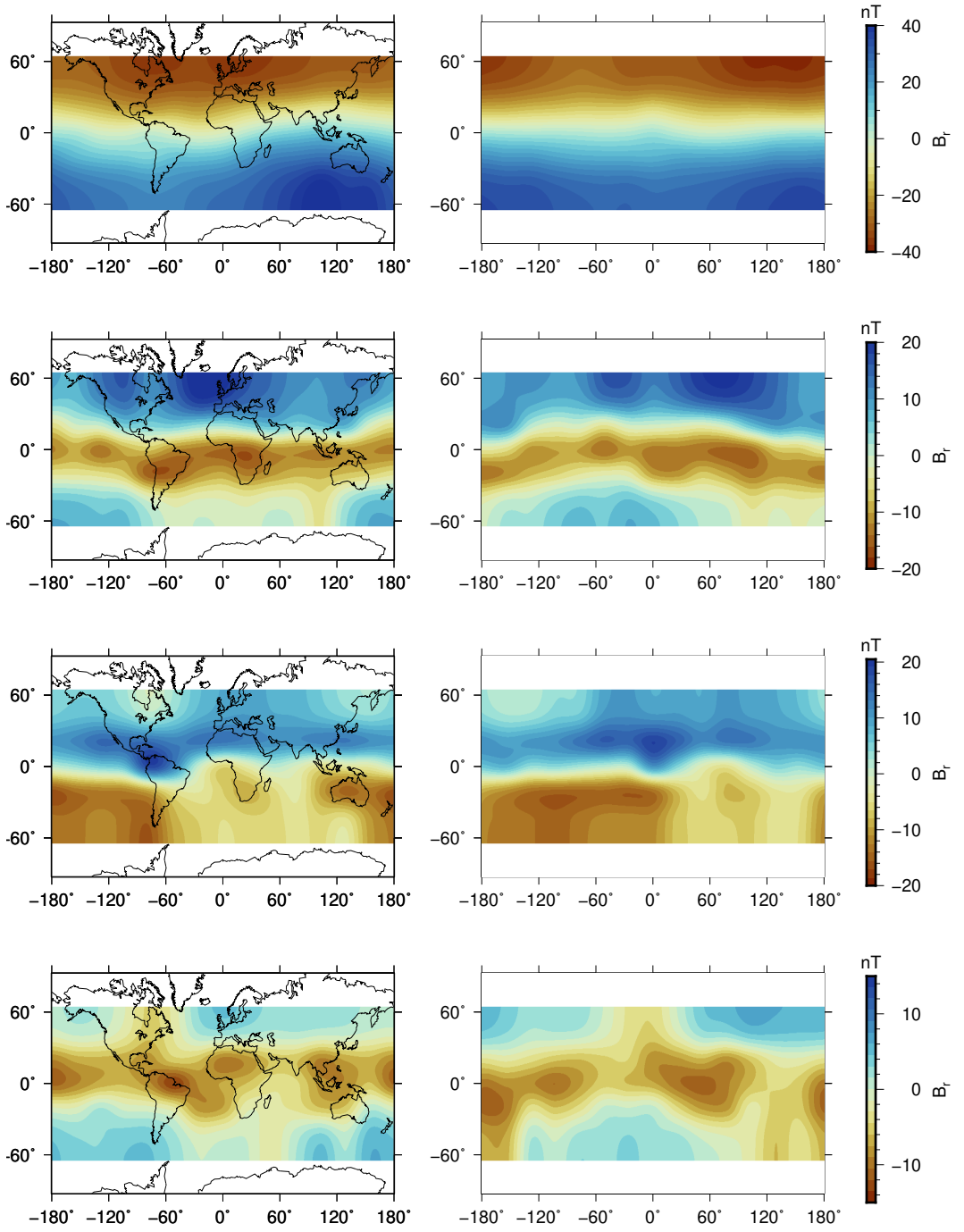

Figure 7. Dimensional EOF spatial structures ($\alpha^j \mathbf{p}^j$) for the radial component of the first 4 modes, both in the GEO (left) and CD (right) frames. j increases from top to bottom. The datasets include only VOs located at $|\Theta_{VO}| \leq 60°$.

$\mathbf{y}^2$, $\mathbf{y}^3$ nor $\mathbf{y}^4$ have significant correlations with any of the proxies in the list. Results for VO'$_{CD}$ (not shown) are very similar to VO'$_{GEO}$.

The small correlation of modes 2, 3 and 4 with Sun-Earth interaction parameters or magnetospheric activity proxies seems to exclude the solar wind or the magnetosphere

	mode 1	mode 2	mode 3	mode 4
	RMS from PCA modes (nT)			
VO'$_{GEO}$	6.81	4.78	3.49	2.41
VO'$_{CD}$	6.10	4.58	3.31	2.22
	Characteristic values (nT)			
VO'$_{GEO}$/ VO'$_{CD}$	$(q_1^0)^{CD} = 23.4$	MAV^{GEO} = 13.4	MAV^{CD}= 5.7	MAV^{GEO} = 6.7

Table 2. For the first four modes j, RMS values of the radial component at the time the maximum of $\mathbf{y}^j$ is attained, over $|\Theta_{VO}| \leq 60°$ region. Also shown, characteristic values computed as explained in the Discussion, for an easier comparison of each mode amplitude with results from other studies.

as the main drivers for those modes. Instead, it suggests that driving processes may lie in the lower atmosphere (e.g. Heelis, 2004).

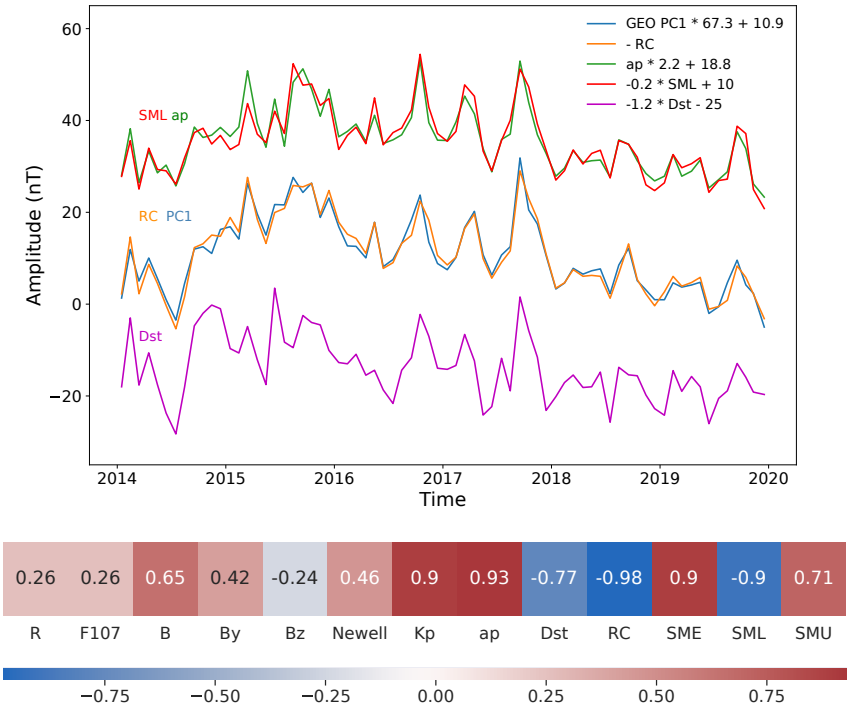

Figure 8. (Top) The $\mathbf{y}^1$ time series (GEO frame) is plotted together with different tested proxies. (Bottom) Pearson correlation coefficients between $\mathbf{y}^1$ time series and different proxies of Sun-Earth interaction (see text). Correlation coefficients have p-value<0.05.

6.2 Comparison with CM6 ionospheric simulations

The power spectrum for mode 2 (Figure 6) reveals a main annual periodicity, followed by 4.5 and 9 months peaks that can be related with Swarm orbital parameters (Figure 1). However, there is no correlation with the solar activity, interplanetary field nor geomagnetic activity indices, just as for modes 3 and 4.

The solar quiet daily vortices are taken into account in the CM comprehensive models (see e.g. Sabaka et al., 2004, 2020). To test the hypothetical relation of mode 2 (and eventually 3 and 4) with those current systems, simulations were computed using CM6. From hourly values of the ionospheric field (both primary and induced), 30-day means were computed on the same grid as for VO'$_{GEO}$, for the whole 2014-2019 period. Then, the PCA decomposition was applied. Two modes explain most of the variability of the simulated ionospheric signal, the second one with spatial symmetry close to VO's mode 2 and time variation with a main annual periodicity and the first one with spatial symmetry close to VO's mode 3 and time variation with a main semiannual periodicity. Figure 9 shows the EOFs and PCs of the first two modes of PCA applied to CM6 ionospheric component.

7 Discussion

Results for the correlation of different $\mathbf{y}^j$ time series with proxies for the solar activity, interplanetary field and magnetospheric variability, support the view that mode 1 describes the variability of magnetospheric currents, contrary to modes 2, 3 and 4. From comparison of these latter modes with CM6, it seems very likely that they are due to the global ionospheric current system responsible for the solar daily variation. A more detailed discussion for each mode follows, based on the results of this study.

7.1 Magnetospheric mode

A dominantly zonal dipolar mode sorts out as the main mode, with a relatively short-term variability (a few months), and irregular amplitude (Figures 6 and 7). Its dipolar geometry, alignment with the CD frame equator and LT-invariance suggest that it may represent the variability of the symmetric ring current with a 30-day time resolution. The well-known semiannual variation (SAV) of geomagnetic activity is clearly present in its power spectrum (see Figure 6). Different mechanisms were proposed to explain SAV, namely the equinoctial, the axial and the Russell-McPherron mechanisms (see e.g. Lockwood et al., 2020, for a recent review). All of them explain how solar-forced external drivers, namely the flux of the solar wind entering the magnetosphere, can be responsible for a 6-months periodicity in magnetospheric currents. A totally different mechanism originates the SAV retrieved in ionospheric modes 2, 3 and 4 discussed below, with origin in atmospheric tidal currents.

Figure 8 shows that RC time series correlates the best with $\mathbf{y}^1$. Nonetheless, both Kp/ap and SML/SME are also highly correlated, clearly above Dst. The RC index parametrizes the ring current activity and, in its most recent version, it is derived from 14 mid and low latitude ground observatories (Finlay et al., 2015). Since a few years ago, it has been considered a better index than Dst to monitorize the ring current activity. As for the ap index, it uses data from 13 mid-latitude stations with geomagnetic dipole latitude close to 50°. SML and SME are auroral electrojet indices that use more than 100 northern hemisphere stations from the SuperMAG collaboration (Gjerloev, 2012), between +40° and +80° geomagnetic dipole latitude. Our results seem to show that, when taking into account high geomagnetic activity levels and to 30-days time resolution, indices ap or SML are also good proxies of the ring current dynamics, probably due to coupling between different external current systems.

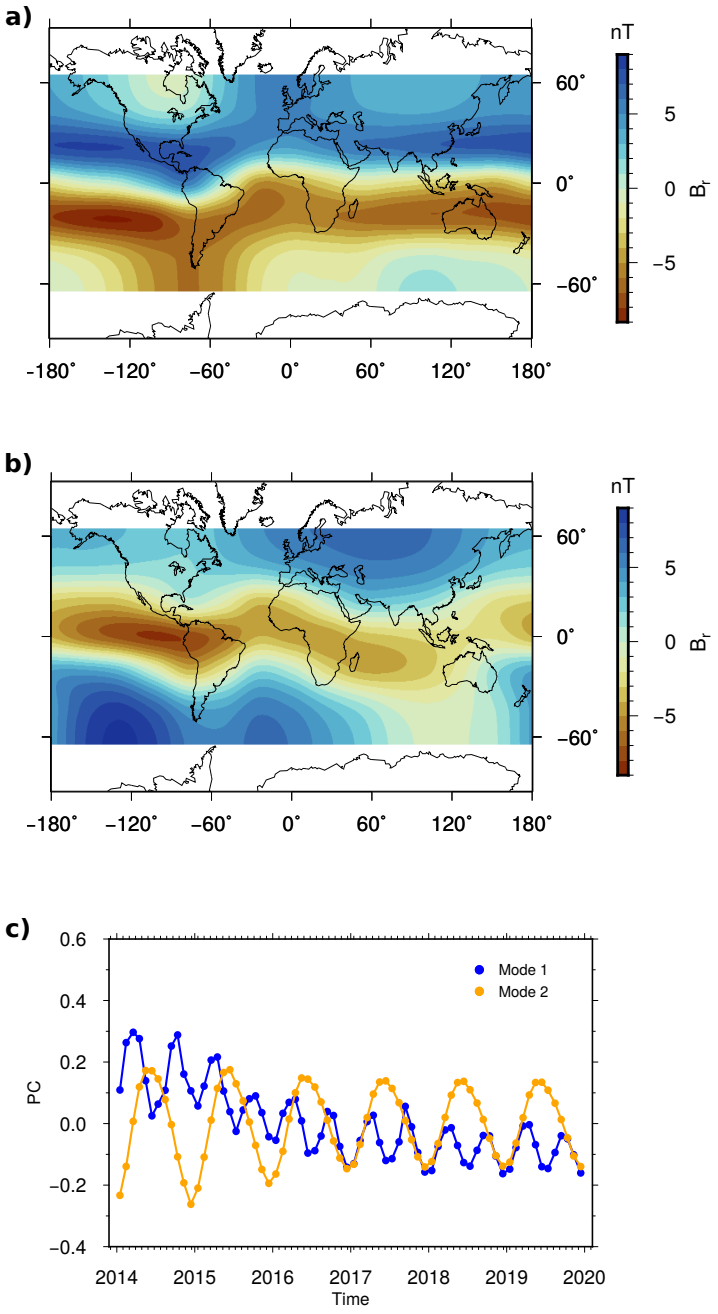

Figure 9. PCA applied to CM6 estimations of the ionospheric component. (a) EOF1; (b) EOF2; (c) PCs.

We now test the value of 6.1 nT in Table 2 for the RMS of B_r in mode 1, against independent results concerning the ring current. A simple model frequently used for the

primary/inducing field is that of a uniform magnetic field derived from a degree-1 external potential, in a spherical harmonic (SH) representation (e.g. Hamilton, 2013), i.e., $\mathbf{B} = q_1^0(\cos\theta\,\hat{e}_r + \sin\theta\,\hat{e}_\theta)$ in the CD frame. Taking into account the corresponding secondary/induced (internal) field, and assuming a frequency independent factor ~ 0.3 relating the induced to the inducing contributions, the radial component at the satellite altitude h is $B_r = \left[0.6(R_E/r)^3 - 1\right] q_1^0 P_1^0(\theta)$, with $r = R_E + h$ (e.g. Yamazaki & Maute, 2017). The q_1^0 SH coefficient would then give directly the intensity of the ring current (uniform) field, aligned with the z-axis of the CD reference frame and pointing from the northern to the southern hemispheres, since the global current is westward. A more precise parameter to compare with the value in Table 2 is the root-mean-square of the radial component of this uniform field, $\left[(1/S)\int B_r^2\, dS\right]^{1/2}$, considering only the region $|\Theta_{VO}| \leq 60^\circ$ and $h = 500$ km in the calculation of surface integrals. This gives $0.261\ q_1^0$. Making this expression equal to our estimate, yields $q_1^0 = 23.4$ nT, a bit lower than values found in Hamilton (2013) or Shore et al. (2016), which were computed for a higher time resolution. A further simplified model allows to relate the magnetic field due to a ring current at its center and the current intensity value I_{RC}. Using for the ring current radius $\sim 4R_E$, leads us to compute $I_{RC} = 8R_E q_1^0/\mu_0$ with 0.95 MA as a result. This is of the right order of magnitude of ring current intensity values (e.g. Prölss, 2004).

7.2 Ionospheric modes

Solar quiet daily vortices have foci at $\pm\ 30^\circ$ of the dip equator (Yamazaki et al., 2011) and originate a field with radial component of different sign in both hemispheres (e.g. Sabaka et al., 2020, Figure 11). The vortices having a maximum at noon LT and practically zero current in the nightime, this radial contribution does not average to zero over both day and night LTs binned inside each VO cylinder. As a result, it will be present for each VO at each epoch, and represented as a spatial structure approximately anti-symmetric relative to the equator.

The spatial structure of the associated variability modes may show the same equatorial anti-symmetry as the time average or a different one, as was also studied by Yamazaki et al. (2009). Because of variable insolation, the ionospheric conductivity at higher latitudes, where the summer-winter difference in the ionization rate is more significant, exhibits a seasonal variation with larger conductivities occurring in the summer hemisphere. The morphology of the corresponding variability mode is an equivalent equatorial symmetric single vortex pattern centered at the equatorial region in the morning sector, with anticlockwise currents around June and clockwise currents around December. The spatial pattern computed by Yamazaki et al. (2009) for the equivalent currents explaining the data has an additional complexity: on the east side of the vortex that extends to large latitudes, currents circulate in the opposite sense and closer to the equator, along a smaller vortex (see Yamazaki et al., 2009, Figure 5). Figure 10 outlines this variability mode. The superposition of an equatorially symmetric mode to the average hemispheric anti-symmetry leads to hemispheric asymmetry in the Sq current system, with stronger current vortices observed in the local summer hemisphere and weaker vortices in the local winter hemisphere, sometimes almost disappearing (e.g. Pedatella et al., 2011; Yamazaki & Maute, 2017). This is the well-known annual oscillation of Sq currents, where the growth of the northern hemispheric vortex occurs simultaneously with the decay of the southern vortex and vice-versa, with maxima and minima at the solstices (see Figure 10). The other main seasonal oscillation that is known to occur has semiannual periodicity (e.g. Yamazaki et al., 2011). During equinoxes, the total current intensity of the Sq current system is maximum due to maxima of its driving tidal winds, propagating from the lower atmosphere. So, there is a semiannual simultaneous growth and decay of the two counter-rotating equivalent current vortices, the radial component of this variability mode showing the same equatorial symmetry as the average pattern (see Figure 10).

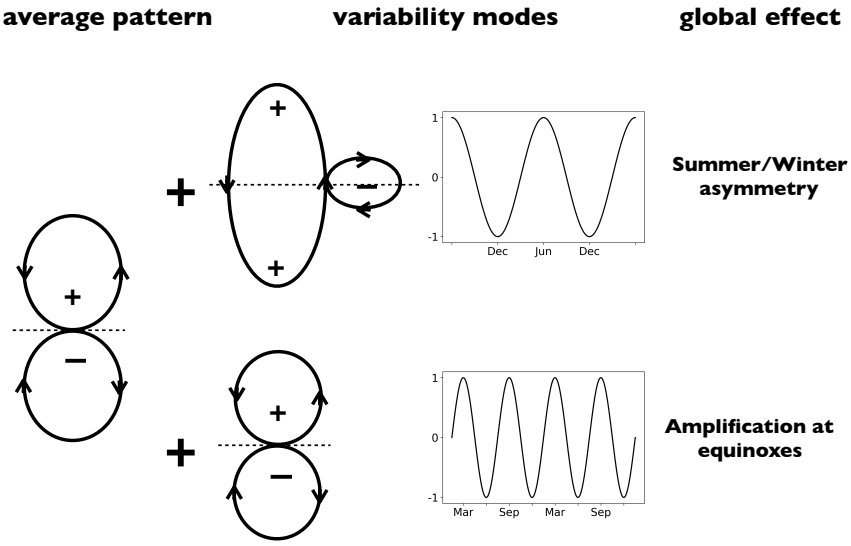

Figure 10. Schematic view of the symmetries and periodicities present in global ionospheric currents' variability. Arrows show the equivalent currents circulation sense at the time the load coefficients in the time series plots are positive. '+' sign for both anticlockwise circulation and radial field pointing outward; '–' sign for the opposite.

Each one of these two periodicities (annual and semiannual) is seen in the PCA modes computed from CM6 simulations (see Figure 9). The two CM6 modes are swapped relative to Yamazaki et al. (2009) and to our own results: the first mode is the semiannual simultaneous growth and decay of the two counter-rotating vortices, displaying an (approximately) anti-symmetric structure relative to the magnetic equator for the radial component and a symmetric structure for the meridional component (not shown); the second mode displays an equatorial symmetry and an annual periodicity consistent with the observed Summer/Winter asymmetric oscillation of the two counter-rotating vortices (see Figure 10).

In our results, the annual variability of mode 2 (Figure 6) and its spatial structure (Figure 7) for the radial component, with features approximately along the equator, can be related to the Summer/Winter oscillation of the global ionospheric current system, as discussed above (see e.g. Yamazaki et al., 2009, 2011; Yamazaki & Maute, 2017). This mode is similar to the Swarm external oscillation that came out from Domingos et al. (2019) study. It also corresponds to CM6 mode 2 (Figure 9).

The Swarm sampling periodicity of 4.5 months is dominant in modes 3 and 4. For mode 3, the 6-months period is the second most important and the similarity of the corresponding EOF to the spatial structure retrieved from the CM6 PCA mode 1 is quite high (Figures 7 and 9). The equivalent current system representation that can explain this mode (see Figure 10) shows close agreement with the equatorial antisymmetric pattern recovered by Yamazaki et al. (2009) to explain semiannual variation (see their Figure 6). This seems to show that the semiannual oscillation of ionospheric current vortices is the main source of variability of mode 3. All these results contribute to an interpretation of modes 2, 3 and possibly mode 4 as variability modes of the current system responsible for the solar daily variation. It remains to comment on the interchange of the two main ionospheric modes in going from CM6 to our (and Yamazaki et al., 2009) calculations. A possible explanation could be an aliasing of the CM6 magnetospheric SAV

into the ionospheric component, thus artificially increasing the semiannual ionospheric variability mode energy.

From PCA results, we now produce estimations for characteristic intensities of the ionospheric signal at 500 km altitude and 30-day time resolution. Its primary sources lie below the VOs altitude, at the E or the F ionospheric layers, and the computed field derives from an harmonic potential with internal sources. The decomposition of this harmonic signal into multipoles would not allow a direct comparison of SH coefficients with existing estimates for the ionospheric field SH coefficients as observed on-ground (below sources). Based on the dominant geometries that sort out from Figure 7, namely P_2^0 for modes 2 and 4 and P_1^0 for mode 3, we use the RMS values in Table 2 to estimate SH coefficients α_1^0 (mode 3) and α_2^0 (modes 2 and 4). Then, from the very simple SH models $B_r = \alpha_n^0 P_n^0$, we compute maximum absolute values (MAV) at the GEO equator for modes 2 and 4, and at $\pm\ 60^0$ CD latitude for mode 3, that can also be found in Table 2. As in section 7.1, surface integrals cover only the region between $\pm\ 60°$ latitude.

7.3 Longitudinal variation

The longitudinal variation seen in modes 2, 3 and 4, with intensity peaks over South America (modes 2, 3 and 4), Africa (modes 2 and 4), Southeast Asia/Australia (modes 2, 3 and 4) or Central Pacific (modes 2, 3 and 4), located along the equatorial region but not particularly along the geomagnetic dipole equator (see Figure 7), could be indicative of the role of certain tidal winds in lower atmosphere-ionosphere coupling (e.g. Oberheide & Forbes, 2008; Lühr et al., 2008). The diurnal eastward propagating tide of zonal wavenumber 3 (DE3) is a nonmigrating tide that can be excited by latent heat release in the tropical troposphere associated with raindrop formation in deep convective clouds (e.g. Oberheide & Forbes, 2008). Tidal winds propagate upward and subsequently contribute to the E-region dynamo. The E-region polarization electric fields can be further transmitted along magnetic field lines into the overlying F-region and drive the dynamo there, too. The longitudinal distribution of convective cloud formation regions concerns the South America, Africa, Southeast Asia, and the central Pacific sectors. A semiannual variability is associated with this structure, with amplification close to equinoxes (e.g. Pedatella et al., 2011). In order to clarify if the effect of nonmigrating DE3 tidal wave could be retrieved in VO series from Swarm data, a further calculation was made. Since during the 2017-2018 period the Swarm sampling is more even in Local Times, it is expected that ionospheric signal could be then retrieved with minimum blurring by the spurious 4.5 month oscillation. The PCA was applied to VO series for the 2-yrs period (Figure 11). Modes 1 and 2 are similar to the two first modes obtained for the whole 2014-2019 duration (Figure 7). However, mode 3 does now clearly show the four-peaked longitudinal structure described above. Its maxima are located at longitudes of about 5°, 115°, 200° and 280°, very close to maxima of different neutral and plasma parameters that are involved in a variety of mechanisms coupling the lower atmosphere to the geospace through the DE3 nonmigrating tide (e.g. Oberheide et al., 2015). The wavenumber-4 structure has been resolved by (Chulliat et al., 2016) also using Swarm data. Here, we confirm the deviation of such structure towards the Southern Hemisphere, as noticed there.

7.4 Comparison with previous results

Previous studies closest to ours are Yamazaki et al. (2009) and Shore et al. (2016), using ground magnetometer data, and Domingos et al. (2019) also using VO series from satellite data. Shore et al. (2016) applied the same non-parametric methods to separate different correlation modes, but they used only data from the internationally defined five magnetically quietest days in each month. We can find correspondence between the three main modes in both studies: a first ring current, a second annual oscillation and a third semiannual ionospheric modes. Their maximum estimate for the q_1^0 coefficient is about two times ours, which can be due to the smoothing effect in the 30-day averages that we

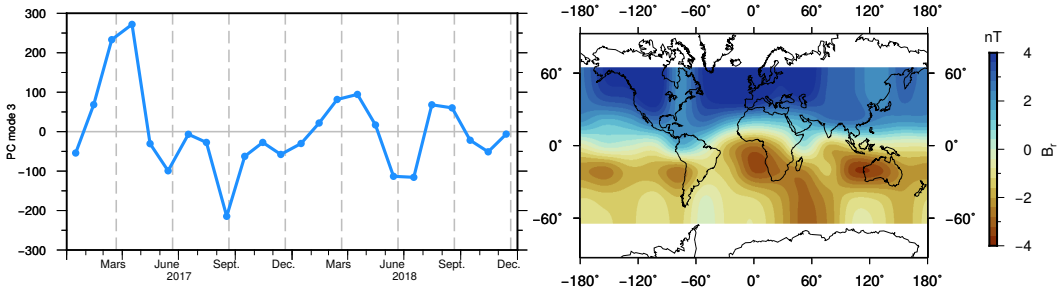

Figure 11. For the 2-year period 2017-2018, the PCA mode 3 (PC on the left, EOF on the right), showing equinoctial amplification of a nearly equatorial four-peaked structure. Vertical lines on the left mark equinoxes and solstices.

use. Their annual oscillation is identified as a 'seasonal motion of the background field', while results from this study allow to identify the annual signal as due to Sq vortex intensity peaking during Summer and Winter at alternating hemispheres. We find in Yamazaki et al. (2009) an explanation of ionospheric modes 2 (annual) and 3 (semiannual) which is closer to ours. Their estimates for the ratio of amplitudes between these two modes are also similar. Finally, in Domingos et al. (2019), strict selection rules and external field modelling applied to eliminate external contributions did not allow to resolve any magnetospheric mode. As a result, the only external mode identified was a residual (peak RMS value of 0.835 nT for the radial component), which nonetheless could resolve the annual periodicity and the quadrupolar pattern of the radial component. In the present study, without any data selection to remove the external field, this mode is recovered with a significantly higher amplitude (RMS of 4.6−4.8 nT). Recently, Hammer et al. (2021) computed 1-month VO time series (called GVO) that account for the whole geomagnetic field signal at satellite altitude. The main differences to our VO series are: the use of the Cartesian cubic potential; the fit to data residuals inside each cylinder; a lower spatial resolution in the global VO mesh with less than one tenth of nodes. Most importantly, VO series in the present study are further examined in search for correlations among them that can be related to the dynamics of external sources, and as a result each VO series can be decomposed into different contributions. In Figure 12, the radial component of the external geomagnetic field at the four VOs above COI, CLF, HER and LRM (see Figure 4) is decomposed into separate and added contributions from PCA modes 1, 2, 3 and 4. As can be seen, VO series are closely represented by the first four modes. As a consequence, this small set of modes seem to explain the most important differences in the external field as seen above different observatories.

8 Conclusion

Starting from a large Swarm dataset that includes measurements during all geomagnetic activity levels in the 2014-2019 period, the VO series computed in this study using the ESD inversion contain a significant external contribution. They can help to bring new insight into the dynamics of the external current systems that contribute the most to variability at the Swarm satellite altitude.

Here, after subtracting to the VO series the main field contribution computed using CHAOS-6, we identified a main PCA mode with spatial geometry suggestive of the magnetospheric ring current system and three modes associated to the mid/low latitude ionospheric current systems. The RC index was identified as the best proxy for the dynamics of mode 1, on a 30-day time resolution, and taking into account all geomagnetic activity conditions. Estimations for parameters characterizing these modes were com-

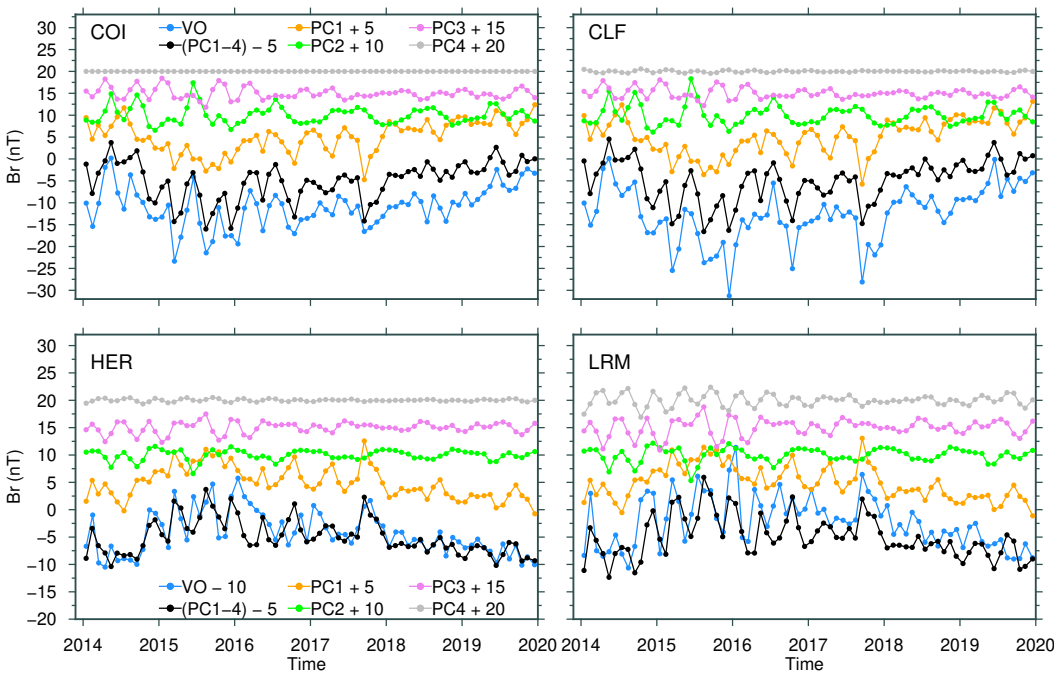

Figure 12. Radial component of VO series and corresponding contributions from the first four PCA modes, at 500 km above the four magnetic observatories COI, CLF, HER and LRM. Separate contributions were shifted vertically, for clarity. PC1-4 is for the sum of the four contributions.

puted, for comparison with results from other studies. In the end, and to illustrate possible applications, the PCA mode decomposition was applied in order to separate contributions from uncorrelated sources in the VO series above on-ground magnetic observatories.

The exploitation of VO series can be further improved. As an example, from comparison with on-ground Earth observatory series, VO series can help to shed light on the height dependence of external currents. A more thorough comparison of the external signals at different altitudes, encompassing a larger number of observatories, was not intended in this study. However, our results seem to show that the ESD method estimations recover the external field signal in a way that is easily comparable with ground observatories series. The observed differences in amplitude and shape of curves, should then carry information on the dependence of external fields with altitude, and on related Earth induced effects, which are seen differently on-ground and at altitude. VO external series could also have a further useful application, in principle, as a means to control on-ground observatories baseline jumps. The set of all N_P=2920 VO series computed in this study has been made available and can be freely used for these or other related applications.

A 4.5-month oscillation due to the average time taken by the satellites to cover all LT values is dominant in modes 3 and 4 (though also present in mode 2), where it hampers a more precise information on currents contributing to these modes' time variation. A straightforward means to get rid of this period would be to bin data using time windows of 4.5 months. But this would prevent to resolve any other signal on monthly timescales,

as is now possible for mode 1. A more interesting solution would be to use a cluster of satellites covering all LTs at all UT times. Meanwhile, by repeating the PCA calculation in the 2017-2018 interval when the amplitude of the 4.5-month oscillation is lower, we could better extract from Swarm data a signal apparently related with the coupling of nonmigrating DE3 tidal wave and the ionosphere. A parameterization of this contribution in geomagnetic field models should probably be considered.

Acknowledgments

The VO series used in this study have been made available at DOI: `https://doi.org/10.5281/zenodo.4515779`. We want to thank Fernando Pinheiro for valuable discussions and comments to the manuscript. We would also like to thank Chris Finlay and Nils Olsen, for providing information on the CM6 model and the MATLAB code to compute the CM6 ionospheric field components. The authors acknowledge ESA for providing access to Swarm Level 1b products (`https://earth.esa.int/eogateway/missions/Swarm/description`); the DTU geomagnetic group for providing access to CHAOS-6 model coefficients (`www.spacecenter.dk/files/magnetic-models/CHAOS-6/`) and to the RC index `http://www.spacecenter.dk/files/magnetic-models/RC/`; the NASA/Goddard Space Flight Center for the access to the OMNI database (`https://omniweb.gsfc.nasa.gov/form/dx1.html`); the Edinburgh World Data Center for Geomagnetism (`http://www.wdc.bgs.ac.uk/catalog/master.html`) and INTERMAGNET for ground observatory data (Macmillan & Olsen, 2013); and the SuperMAG collaborators (`https://supermag.jhuapl.edu/info/?page=acknowledgement`) for SML, SMU and SME indices (`https://supermag.jhuapl.edu/indices/`). Figures were produced using GMT (Wessel et al., 2013). This study is funded by national funds through FCT (Foundation for Science and Technology, I.P.), under project MAG-GIC: PTDC/CTA-GEO/31744/2017. CITEUC is funded by FCT (UIDB/00611/2020 and UIDP/00611/2020). D.S. is supported by CNES within the project "Exploitation des mesures de la mission Swarm".

References

Barrois, O., Hammer, M. D., Finlay, C. C., Martin, Y., & Gillet, N. (2018). Assimilation of ground and satellite magnetic measurements: inference of core surface magnetic and velocity field changes. *Geophys. J. Int.*, *215*, 695–712. doi: https://doi.org/10.1093/gji/ggy297

Beggan, C. D., Whaler, K. A., & Macmillan, S. (2009). Biased residuals of core flow models from satellite-derived 'virtual observatories'. *Geophys. J. Int.*, *177*, 463–475.

Bezděk, A., Sebera, J., & Klokočník, J. (2017, May). Validation of Swarm accelerometer data by modelled nongravitational forces. *Advances in Space Research*, *59*(10), 2512-2521. doi: 10.1016/j.asr.2017.02.037

Capderou, M. (2005). *Satellites: Orbits and missions*. Springer.

Chulliat, A., Vigneron, P., & Hulot, G. (2016, June). First results from the Swarm Dedicated Ionospheric Field Inversion chain. *Earth, Planets, and Space*, *68*, 104. doi: 10.1186/s40623-016-0481-6

Domingos, J., Pais, M. A., Jault, D., & Mandea, M. (2019). Temporal resolution of internal magnetic field modes from satellite data. *Earth, Planets, and Space*, *71*(1), 2. doi: 10.1186/s40623-018-0983-5

Finlay, C. C., Olsen, N., Kotsiaros, N., Gillet, N., & Tøffner-Clausen, L. (2016). Recent geomagnetic secular variation from *Swarm* and ground observatories as estimated in the CHAOS-6 geomagnetic field model. *Earth Planets Space*, *68*(112). doi: 10.1186/s40623-016-0486-1

Finlay, C. C., Olsen, N., & Tøffner-Clausen, L. (2015, July). DTU candidate field models for IGRF-12 and the CHAOS-5 geomagnetic field model. *Earth, Planets, and Space*, *67*, 114. doi: 10.1186/s40623-015-0274-3

Friis-Christensen, E., Lühr, H., & Hulot, G. (2006, April). Swarm: A constellation to study the Earth's magnetic field. *Earth, Planets, and Space*, *58*, 351-358.

Gjerloev, J. W. (2012, September). The SuperMAG data processing technique. *Journal of Geophysical Research (Space Physics)*, *117*(A9), A09213. doi: 10.1029/2012JA017683

Hamilton, B. (2013, November). Rapid modelling of the large-scale magnetospheric field from Swarm satellite data. *Earth, Planets, and Space*, *65*(11), 1295-1308. doi: 10.5047/eps.2013.09.003

Hammer, M. D. (2018). *Local estimation of the earth's core magnetic field* (Unpublished doctoral dissertation). Ph.D. thesis, Technical University of Denmark.

Hammer, M. D., Cox, G. A., Brown, W. J., Beggan, C. D., & Finlay, C. C. (2021, December). Geomagnetic Virtual Observatories: monitoring geomagnetic secular variation with the Swarm satellites. *Earth, Planets, and Space*, *73*(1), 54. doi: 10.1186/s40623-021-01357-9

Heelis, R. A. (2004, July). Electrodynamics in the low and middle latitude ionosphere: a tutorial. *Journal of Atmospheric and Solar-Terrestrial Physics*, *66*(10), 825-838. doi: 10.1016/j.jastp.2004.01.034

Jolliffe, I. T. (2002). *Principal Component Analysis, second edition.* New York: Springer-Verlag.

Langlais, B., Purucker, M. E., & Mandea, M. (2004). Crustal magnetic field of mars. *J. Geophys. Res*, *109*, E02008.

Laundal, K., & Richmond, A. D. (2017). Magnetic coordinate systems. *Space Sci. Rev.*, *206*(1–4), 27–59.

Lockwood, M., Owens, M. J., Barnard, L. A., Haines, C., Scott, C. J., McWilliams, K. A., & Coxon, J. C. (2020, May). Semi-annual, annual and Universal Time variations in the magnetosphere and in geomagnetic activity: 1. Geomagnetic data. *Journal of Space Weather and Space Climate*, *10*, 23. doi: 10.1051/swsc/2020023

Lühr, H., Rother, M., HäUsler, K., Alken, P., & Maus, S. (2008, August). The influence of nonmigrating tides on the longitudinal variation of the equatorial electrojet. *Journal of Geophysical Research (Space Physics)*, *113*(A8), A08313. doi: 10.1029/2008JA013064

Lühr, H., Xiong, C., Olsen, N., & Le, G. (2017). Near-earth magnetic field effects of large-scale magnetospheric currents. *Space Science Reviews*, *206*(1-4), 521–545.

Lühr, H., & Zhou, Y.-L. (2020, June). Residuals to the CHAOS-6 Geomagnetic Field Model Caused by Magnetospheric Currents During Enhanced Magnetic Activity. *Geochemistry, Geophysics, Geosystems*, *21*(6), e08976. doi: 10.1029/2020GC008976

Macmillan, S., & Olsen, N. (2013). Observatory data and the Swarm mission. *Earth, Planets and Space*, *65*(11), 1355–1362.

Mandea, M., & Olsen, N. (2006). A new approach to directly determine the secular variation from magnetic satellite observations. *Geophys. Res. Lett.*, *33*(L15306).

Mayhew, M. A. (1979). Inversion of satellite magnetic anomaly data. *Geophys. J.*, *45*, 119128.

Montenbruck, O., & Rodríguez, B. G. (2020). NeQuick-G performance assessment for space applications. *GPS Solutions*, *24*, 13. doi: 10.1007/s10291-019-0931-2

Newell, P. T., & Gjerloev, J. W. (2011, December). Evaluation of SuperMAG auroral electrojet indices as indicators of substorms and auroral power. *Journal of Geophysical Research (Space Physics)*, *116*(A12), A12211. doi: 10.1029/2011JA016779

Newell, P. T., Sotirelis, T., Liou, K., Meng, C. I., & Rich, F. J. (2007, January). A nearly universal solar wind-magnetosphere coupling function inferred from

10 magnetospheric state variables. *Journal of Geophysical Research (Space Physics)*, *112*(A1), A01206. doi: 10.1029/2006JA012015

North, G. R., Bell, T. L., Cahalan, R. F., & Moeng, F. J. (1982). Sampling errors in the estimation of empirical orthogonal functions. *Mon. Wea. Rev.*, *110*, 699-706.

Oberheide, J., & Forbes, J. M. (2008, February). Tidal propagation of deep tropical cloud signatures into the thermosphere from TIMED observations. *Geophysical Research Letters*, *35*(4), L04816. doi: 10.1029/2007GL032397

Oberheide, J., Shiokawa, K., Gurubaran, S., Ward, W. E., Fujiwara, H., Kosch, M. J., ... Takahashi, H. (2015, December). The geospace response to variable inputs from the lower atmosphere: a review of the progress made by Task Group 4 of CAWSES-II. *Progress in Earth and Planetary Science*, *2*, 2. doi: 10.1186/s40645-014-0031-4

Oliveira, J. S., Langlais, B., Pais, M. A., & Amit, H. (2015). A modified Equivalent Source Dipole method to model partially distributed magnetic field measurements, with application to Mercury. *Journal of Geophysical Research (Planets)*, *120*(6), 1075-1094. doi: 10.1002/2014JE004734

Olsen, N., Lühr, H., Finlay, C. C., Sabaka, T. J., Michaelis, I., Rauberg, J., & Tøffner-Clausen, L. (2014). The CHAOS-4 geomagnetic field model. *Geophys. J. Int.*, *197*(2), 815-827.

Park, J., Yamazaki, Y., & Lühr, H. (2020). Latitude dependence of interhemispheric field-aligned currents (ihfacs) as observed by the swarm constellation. *Journal of Geophysical Research: Space Physics*, *125*(2), e2019JA027694. Retrieved from `https://agupubs.onlinelibrary.wiley.com/doi/abs/10.1029/2019JA027694` (e2019JA027694 2019JA027694) doi: https://doi.org/10.1029/2019JA027694

Pedatella, N. M., Forbes, J. M., & Richmond, A. D. (2011). Seasonal and longitudinal variations of the solar quiet (sq) current system during solar minimum determined by champ satellite magnetic field observations. *Journal of Geophysical Research: Space Physics*, *116*(A4). doi: https://doi.org/10.1029/2010JA016289

Prölss, G. W. (2004). *Physics of the Earth's Space Environment: an introduction.* Springer.

Purucker, M. E., Sabaka, T. J., & Langel, R. A. (1996, January). Conjugate gradient analysis: A new tool for studying satellite magnetic data sets. *Geophys Res Lett*, *23*(5), 507-510. doi: 10.1029/96GL00388

Sabaka, T. J., Olsen, N., & Purucker, E. (2004). Extending comprehensive models of the Earth's magnetic field with Ørsted and CHAMP data. *Geophys. J. Int.*, *159*, 521-547.

Sabaka, T. J., Tøffner-Clausen, L., Olsen, N., & Finlay, C. C. (2020). CM6: a comprehensive geomagnetic field model derived from both champ and swarm satellite observations. *Earth, Planets and Space*, *72*(1), 1–24.

Saturnino, D., Langlais, B., Amit, H., Civet, F., Mandea, M., & Beucler, E. (2018). Combining virtual observatory and equivalent source dipole approaches to describe the geomagnetic field with Swarm measurements. *Phys. Earth Planet. Inter.*, *276*, 118–133.

Shore, R. M. (2013). *An improved description of earths external magnetic fields and their source regions using satellite data* (Unpublished doctoral dissertation). The University of Edinburgh.

Shore, R. M., Whaler, K. A., Macmillan, S., Beggan, C., Velímský, J., & Olsen, N. (2016). Decadal period external magnetic field variations determined via eigenanalysis. *J. Geophys. Res. Space Physics*, *121*, 5172-5184.

Toffner-Clausen, L., & Nielsen, J. B. (2018). *Swarm Level 1b Product Definition, SW-RS-DSC-SY-0007, Issue 5.22.* `https://earth.esa.int/documents/10174/1514862/Swarm_L1b_Product_Definition/`. ([Online; accessed 3-

March-2020])

Wessel, P., Smith, W. H. F., Scharroo, R., Luis, J., & Wobbe, F. (2013). Generic mapping tools: Improved version released. *Eos, Transactions American Geophysical Union*, *94*(45), 409–410. doi: 10.1002/2013EO450001

Yamazaki, Y., & Maute, A. (2017, March). Sq and EEJ—A Review on the Daily Variation of the Geomagnetic Field Caused by Ionospheric Dynamo Currents. *Space Science Reviews*, *206*(1-4), 299-405. doi: 10.1007/s11214-016-0282-z

Yamazaki, Y., Yumoto, K., Cardinal, M. G., Fraser, B. J., Hattori, P., Kakinami, Y., ... Yoshikawa, A. (2011, October). An empirical model of the quiet daily geomagnetic field variation. *Journal of Geophysical Research (Space Physics)*, *116*(A10), A10312. doi: 10.1029/2011JA016487

Yamazaki, Y., Yumoto, K., Uozumi, T., Yoshikawa, A., & Cardinal, M. G. (2009, December). Equivalent current systems for the annual and semiannual S_q variations observed along the 210^{o}MM CPMN stations. *Journal of Geophysical Research (Space Physics)*, *114*(A12), A12320. doi: 10.1029/2009JA014638